



Electrolyte design for Li metal-free Li batteries

Ji Chen ^{1,†}, Qin Li ^{1,†}, Travis P. Pollard ², Xiulin Fan ¹, Oleg Borodin ^{2,*},
Chunsheng Wang ^{1,3,*}

¹ Department of Chemical and Biomolecular Engineering, University of Maryland College Park, MD 20740, USA

² Battery Science Branch, Energy and Biomaterials Division, Sensors and Electron Devices Directorate, U.S. Army Combat Capabilities Development Command Army Research Laboratory, Adelphi, MD 20783, USA

³ Department of Chemistry and Biochemistry, University of Maryland College Park, MD 20740, USA

Li metal, with the lowest thermodynamically achievable negative electrochemical potential and the highest specific capacity (3860 mAh g^{-1}), is the ultimate anode choice for Li batteries. However, the highest reported Li plating/stripping Coulombic efficiency (CE) of 99.5% after extensive efforts is still too low for the Li metal-free (all the Li metal in cycling comes from cathode, without anode pre-lithiation) Li metal batteries. The low CE is attributed to both non-uniform Li plating/stripping on the lithiophobic Cu current collector and Li dendrite growth through lithiophilic organic-inorganic solid electrolyte interphase (SEI) formed in carbonate electrolytes. Here, we use a lithiophilic Bismuth graphite blend (Bi-Gr) substrate to replace lithiophobic Cu current collector to seed a uniform Li nucleation, and form a lithiophobic LiF-rich SEI rather than lithiophilic organic-rich SEI to suppress Li dendrite growth. Molecular dynamics simulations reveal the preferential reduction of anions in 2.0 M LiPF₆ in tetrahydrofuran/2-methyl tetrahydrofuran (2.0 M LiPF₆-mixTHF) electrolyte to generate LiF-rich SEI on plated Li. Bi-Gr substrate and 2.0 M LiPF₆-mixTHF electrolyte enable the Li anodes to achieve a record high CE of 99.83% at a high capacity of 1.0 mAh cm^{-2} and current of 0.5 mA cm^{-2} . The Bi particles serve as dispersed nucleation centers that promote uniform Li deposition with strong adhesion to the substrate to avoid dead Li, while the lithiophobic LiF-rich SEI promotes lateral Li growth and suppresses the vertical Li dendrite growth even at a high current density of 3.0 mA cm^{-2} and high areal capacities of 3.0 mAh cm^{-2} . The regulation of Li nucleation and growth enables the Li metal-free LiFePO₄ full cells to achieve 100 cycles at a practical areal capacity of $>2.0 \text{ mAh cm}^{-2}$. This manuscript highlights the benefits of simultaneous substrate design to improve Li nucleation and electrolyte design to promote lithiophobic SEI growth, enabling a promising and practical route Li metal-free Li metal batteries.

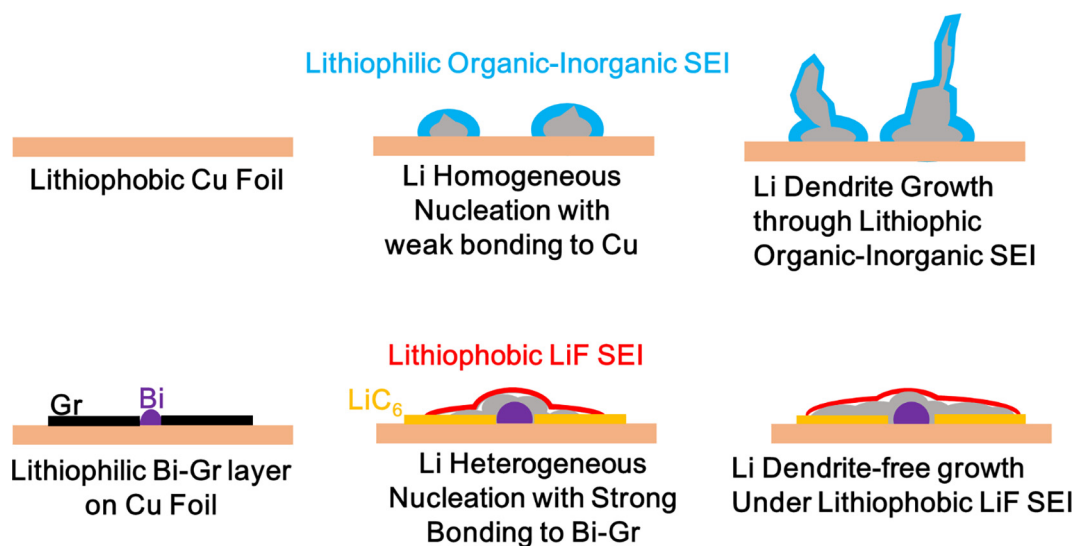
Introduction

An ever-growing energy demand from multiple sectors has reinvigorated research into rechargeable Li metal batteries due to the lowest thermodynamically achievable negative electrochemical potential of Li metal and the highest specific capacity (3860 mAh g^{-1}) [1]. However, the highest reported Li plating/

* Corresponding authors.

E-mail addresses: Borodin, O. (oleg.a.borodin.civ@mail.mil), Wang, C. (cswang@umd.edu).

† These authors contributed equally to this work.

**SCHEME 1**

Difference between traditional and proposed design principle for Li metal substrate and SEI.

stripping Coulombic efficiency (CE) of <99.5% is still too low for practical applications, especially for Li metal-free full cells that do not have lithium excess. The limitations on CE are due to both solid electrolyte interphase (SEI) and substrate. Strong adhesion between Li and the organic-rich SEI that formed during cycling in conventional carbonate electrolytes promotes dendritic growth. While the Cu current collector fails to provide strong adhesion with the deposited Li. The former issue still occurs in recently proposed polymer-inorganic SEI designs that are similarly rich in organic content [2]. A strong Li|SEI adhesion is undesirable as it undermines the mechanical strength of the SEI and undergoes large volume changes that induce cracking and other mechanical defects that promote Li dendrite growth/“dead Li” (Scheme 1, upper row) [3,4]. Additionally, strong adhesion coincides with a low interface energy (strongly wetting), promoting Li penetration through organic-rich SEI to form Li dendrites and reduce Li plating/stripping CE. Thus effective strategies for improving Li plating/stripping CE should adopt a lithiophilic substrate on the current collector to promote a more uniform Li deposition and the SEI should be lithiophobic to resist deformation upon Li volume change and suppress Li dendrite growth (Scheme 1, lower row). The lithiophilic substrate ensures that Li is uniformly plated/stripped [5]. The lithiophobic SEI with high interface energy and weak bonding to Li facilitates Li metal migration at the SEI|Li interface without forcing the lithiophobic SEI to move with Li, thus reducing the stress/strain of lithiophobic SEI. As a result, the lithiophobic SEI retains its mechanical strength and promotes lateral deposition of the Li. Therefore, the combination of lithiophilic substrate and lithiophobic SEI should overcome existing limitations in Li plating/stripping to improve CE and cycle life. However, the combination of both approaches at once has not been explored previously.

Many substrates utilizing different Li-host materials [6] with 3D structures [7] have been investigated to enhance the Li plating/stripping efficiency. To accommodate the large volume changes of Li during plating/stripping cycles and reduce the

actual areal current density, these lithiophilic substrates normally have large surface area (porous carbon [8], graphene [9], etc.), resulting in a low initial CE. Therefore, the ideal lithiophilic substrates should be dense with less surface area and coordinate with lithiophobic SEI to enhance the Li plating/stripping CE.

Among reported components of SEI, LiF is lithiophobic, with high interface energy and weak binding to Li, thus can minimize SEI deformation with volume change on cycling [10]. Additionally, LiF is mechanically strong and so restricts Li growth under SEI|Li interface while preventing Li from penetrating the interface. Thus LiF-rich SEI is best suited for Li dendrite suppression as evidenced by the highest Li plating/stripping CE of 99.5% in localized high-concentration electrolytes [11], all-fluorinated electrolyte [12] and high concentration LiFSI-doped electrolyte [13]. CE in these electrolytes is limited by the similar reduction potentials of fluorinated salts and solvents which still generate some organic components in the SEI, compromising the LiF-rich SEI as described above. Herein, we used a 2.0 M LiPF₆ in tetrahydrofuran (THF) and 2-methyl tetrahydrofuran (MTHF) electrolyte to form LiF/organic bilayer SEI. In combination, a dense and highly lithiophilic graphite-Bi composite substrate was employed to improve the adhesion between Li and substrate (Scheme 1, lower row). When the potential of graphite-Bi electrodes gradually decrease from open-circuit to Li plating potential, the low solvent reduction potential of the ether solvents compared to the fluorinated LiPF₆ salt ensures a nearly pure LiF inner layer evolves that is in contact with Li, with minor polymerized organic products due to ether decomposition in the outer layer (LiF/organic bilayer) [14]. This bilayer SEI model differs from the previously reported organic-inorganic composite SEI where the LiF and organic products are intermixed. The principle behind the formation of LiF/organic bilayer SEI is that the low solvating strength of the ethers in 2 M LiPF₆ in THF:MTHF (1:1 volume, denoted as mixTHF) promotes the formation of contact ion pairs and salt aggregation leading to their preferential reduction to form LiF. The mixture is used for chemical

stability of the electrolyte: single MTHF cannot provide enough solvation, while single THF will be polymerized by Lewis acid (PF_5) from salt. In addition, the high reduction stability suppresses the reduction of mixTHF to form organic SEI. After formation of LiF/organic bilayer SEI, Li accumulates initially at the dispersed Bi particles, overcoming a nucleation barrier observed on graphite substrate alone. The Li and Bi reversibly form Li-Bi alloys that seed further lateral/radial Li deposition and lead to a more uniform deposition across the substrate surface. With the synergetic regulation of Li nucleation on lithiophilic Bi-Gr substrate and non-dendritic growth under lithiophobic LiF-rich SEI, the Li plating/stripping CE in Li metal||Bi-Gr half cells reached the highest recorded CE over 99.8%+ at 0.5 mA cm^{-2} and 1.0 mAh cm^{-2} . The Li metal-free $\text{LiFePO}_4||\text{Bi-Gr}$ full cells with practical areal capacity $>2.0 \text{ mAh cm}^{-2}$ can be cycled for 100 cycles.

Results

Electrolyte design to form LiF-rich SEI

Recent research has demonstrated that increasing the LiF content in organic-inorganic SEI by adding either fluorinated solvents (e.g., FEC) or salts (e.g., lithium bis(fluorosulfonyl)imide, LiFSI) into commercial carbonate electrolytes can suppress Li dendrites [15]. However, the organic content in organic-inorganic SEI, especially near the anode, is still high because of the simultaneous reduction of the fluorinated solvents and LiFSI which generates some organic species as well. Different from LiFSI and LiTFSI salts, the reduction of LiPF_6 salt via electrochemical reduction of salt aggregates [16] or via electro-catalytic HF-based pathway [17] can form LiF without organic components. An alternative approach is to select thermodynamically more stable solvents with low solvent reduction potential, promoting reduction of LiPF_6 salt and minimizing the organic content of the SEI. Increasing LiPF_6 concentration to form high salt aggregation can further reduce organic content in the SEI by preferential reduction of LiPF_6 . High salt aggregation is needed in order to stabilize an excess electron on PF_6^- , thus promoting its preferential reduction and LiF formation. By screening multiple solvents including ester/ether, we selected THF and MTHF, which best satisfies the above requirements due to their low reduction potential, good conductivity $\sim 5.4 \text{ mS/cm}$ (at 2.0 M) and high LiPF_6 solubility up to 2.7 M. The 2.0 M LiPF_6 -mixTHF electrolyte has very high Li^+ transference number (t_+) of 0.74 from experiments and 0.68–0.73 from molecular dynamics (MD) simulations (Table S1), which are much higher than that of the concentrated linear glymes doped with lithium bis(trifluoromethanesulfonyl) imide (LiTFSI) [18] and dual salt electrolyte (LiTFSI:LiFSI/DME) [19]. The high Li^+ transference number (t_+) is beneficial for suppression of Li dendrite growth during lithium metal deposition [14].

Born Oppenheimer Molecular Dynamics (BOMD) simulations using a setup shown in Fig. 1a and S1 provided mechanistic insight into the initial stages of electrolyte reduction and formation of LiF/organic bilayer SEI in the 2.0 M LiPF_6 -mixTHF electrolyte. The simulations included three critical factors needed to realistically represent electrolyte reactivity at electrodes: (1) explicit description of the substrate – electrolyte interactions;

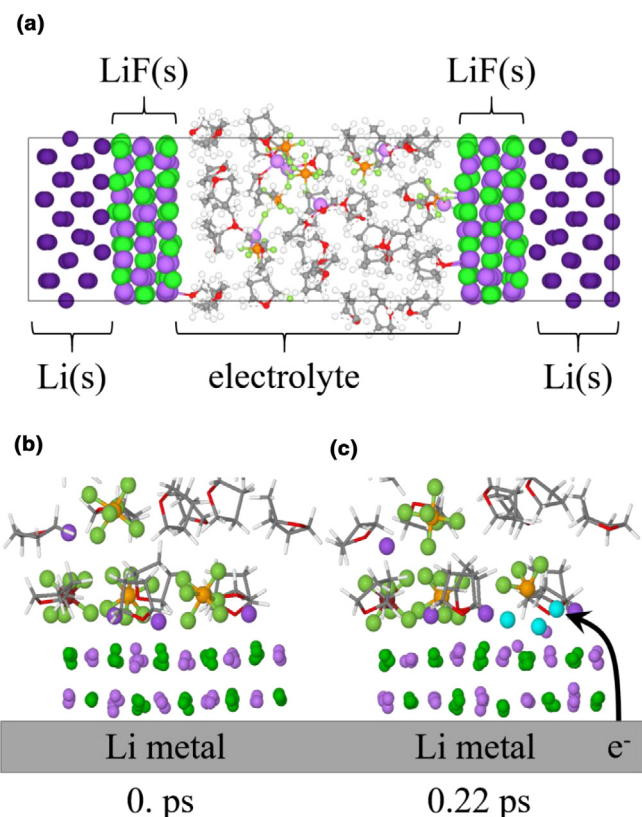


FIGURE 1

Preferential reduction of LiPF_6 salt and LiF generation at the passivated Li metal. (a) A simulation cell used for examination of electrolyte reduction with recoloring/resizing to emphasize certain regions, see Fig. S1 for additional details; (b and c) snapshots from BOMD simulations showing a representative reduction of a PF_6^- anion positioned near the $\text{LiF}|\text{Li}$ surface at the beginning of the simulation (b) 0 picoseconds/ps and (c) after 0.22 ps of BOMD simulations showing LiPF_6 reduction with 3F^- (shown in cyan) abstracted and forming LiF and partial Li^+ vacancies in the model LiF solid electrolyte interphase.

(2) accurate representation of electrolyte structure, ion pairing and aggregation near an electrode; and (3) collection of sufficient statistics from multiple unique simulations that were initiated with differing initial configurations. As stated earlier, a thin layer of LiF will be formed on plated Li when potential drop from open-circuit to Li plating potential. Thus, we choose a 9-layer Li (0 0 1) slab that was capped with trilayers of LiF to simulate electrolyte reduction at the partially passivated Li metal with specific LiF – electrolyte interactions included. A validated polarizable force field (APPLE&P) (see Table S1) was used to prepare 10 representative initial configurations for BOMD DFT simulations that lasted 24 ps and allowed us to capture sufficient statistics for the most frequently observed electrolyte reduction events. Detailed description of the reduction events and movies of the resulting simulations are attached in SI.

In all 10 simulations (denoted as replicas R-1, ..., R-10) no THF or MTHF decomposition nor HF formation was observed. Instead, LiF formation was observed as a result of the $\text{Li}_x(\text{PF}_6)$ ion pair ($x = 1$) or aggregate ($x > 1$) reduction on a timescale of $<10 \text{ ps}$, confirming a strong preference for LiPF_6 vs. solvent reduction. Fig. 1(b and c) shows one of the observed reduction

events when a PF_6^- coordinated to Li^+ cations from the electrolyte and LiF surface undergoes defluorination and formation of 3LiF and PF_3 gas. In a number of cases, Li^+ was too scarce at the interface and could not be liberated from the LiF fast enough to form PF_3 . This led to the evolution of an intermediate, loosely bound PF_4^- anion, observed in previous simulation studies [20]. Because the evolved gases are trapped in our simulations, we saw additional reactivity of PF_3 and PF_4^- species to PF_2 neutral and anionic species. This reaction is not expected to occur if these gases are released. In 3 of the 10 trajectories, a F^- vacancy evolved during the polarizable force field preparation and was carried over to DFT to examine how reactivity changed near surface defects. In each case, a PF_6^- is reduced during our equilibration phase to fill the vacancy and decomposes to PF_3 or the diffuse PF_4^- anion. In each of these simulations, the defective surface led to a high population of PF_6^- (in trajectories R-2, R-8, and R-10, 3 of 6 PF_6^- are on the surface near the defect), suggesting the anions will tend to aggregate near certain defective sites and other imperfections. Our simulations suggest under such conditions, there is a preference for the reduction of the anion to repair the SEI over solvent. Interestingly, as BOMD simulations progressed and multiple electron transferred from lithium metal to electrolyte reducing Li_xPF_6 , we observed a number of fast diffusion events for F^- from the electrolyte|LiF interface to the LiF-lithium metal interface that would be expected to occur during Li stripping, see Fig. S1-f-i. For the sake of brevity here, a more thorough examination and summary of the simulations is provided in the additional discussion in the SI and in Table S2. We conclude that strong LiPF_6 aggregation near the passivated Li metal electrode favors LiPF_6 decomposition leading to the self-limiting LiF SEI growth without any observed solvent reduction.

The formation of LiF-rich SEI layer on the Li metal in LiPF_6 -mixTHF electrolyte was confirmed using X-ray photoelectron spectroscopy (XPS). The typical elemental contribution to the SEI is shown in the pentagon (Fig. 2). It is obvious that SEI from LiPF_6 -mixTHF electrolyte is rich in F but poor in C, consistent with the simulation results that LiPF_6 preferentially decomposes on Li, generating LiF-rich SEI. In contrast, solvent decomposition in LiPF_6 -EC/DMC electrolyte dominates the SEI formation process, evolving a C-rich, F-poor SEI. High resolution F 1s, C 1s with Ar^+ sputtering also supports this conclusion. It is clear that F content remains high but C content diminishes after 120 s, indicating the inner part of SEI generated from LiPF_6 -mixTHF electrolyte is even richer in F and poorer in C. Whilst the C signal remains strong after 120 s sputtering in the SEI from LiPF_6 -EC/DMC electrolyte. From the previous discussion, LiF-rich SEI is effective in regulating the Li growth morphology and improving CE.

Electrochemically, the significantly increased CE from ~86.0% in LiPF_6 -EC/DMC to 99.2% in LiPF_6 -mixTHF at a current of 0.5 mA cm^{-2} and a capacity of 1.0 mAh cm^{-2} in $\text{Li}||\text{Cu}$ half cells (Fig. S2a-c) verified the electrolyte design principle that formation of LiF-rich SEI on Li can improve Li plating/stripping CE. This CE is among the best values reported for $\text{Li}||\text{Cu}$ half cells with similar testing conditions. The CE remains stable for over 100 cycles in the LiPF_6 -mixTHF cells, while for the cell in LiPF_6 -EC/DMC, the CE decreases with cycling due to the insufficient electrode passivation and buildup of ‘dead Li’ that is electrically

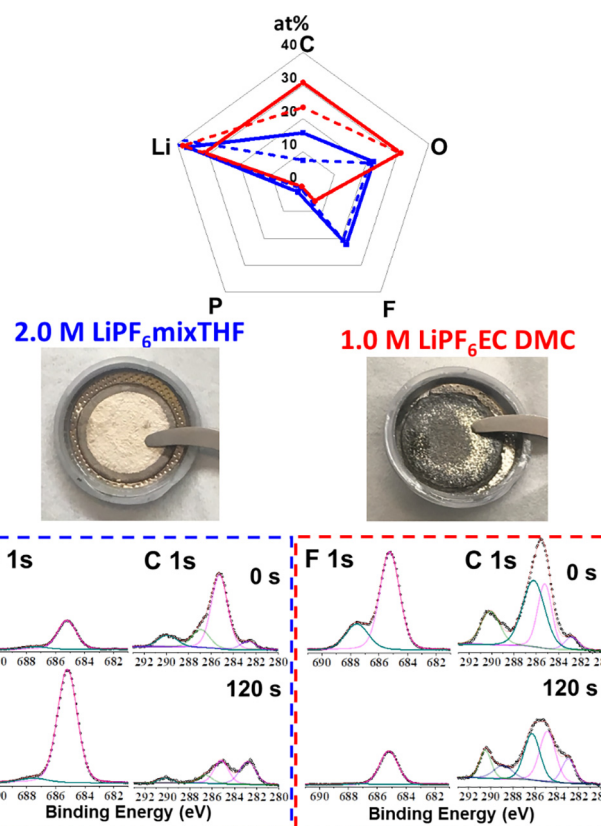


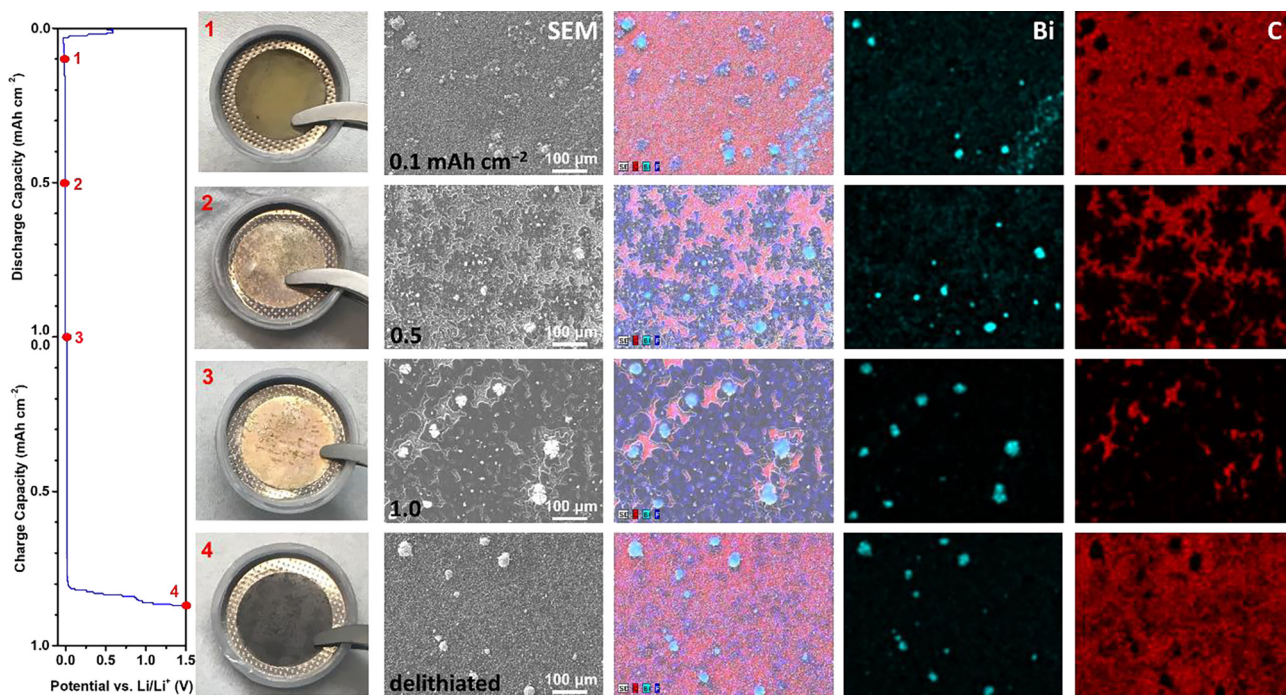
FIGURE 2

Elemental composition and high-resolution XPS F 1s and C 1s spectra of Li cycled in LiPF_6 -mixTHF (blue) or EC/DMC (red). Solid lines denote initial elemental composition, dashed lines – after 120 s of sputtering. Electrolytes, photos are cycled Li after disassembly of cells.

insulated from the anode. Despite these improvements, a 99.2% CE is not high enough for Li anode free full cells with limited Li source from cathodes and complete Li plating/stripping cycles. This is partially because the high lithiophobicity of Cu may detach deposited Li, forming dead Li, especially at the near-to complete Li stripping stage, and could not be improved even with building of 3D and sub-micron Cu structures [6]. To further increase the CE, we designed a special substrate with lower Li nucleation barrier and high Li affinity to provide better adhesion and efficiency.

Substrate design for high Li plating/stripping CE

Carbon substrates have been extensively investigated for Li metal deposition, owing to their high surface area to reduce local current density and Li affinity to improve adhesion of Li metal. Substitution of Cu foil with carbon substrates featuring large specific surface area (e.g., carbon-fiber paper [21], porous graphene network [22], and coating carbon materials onto Cu foil) has been demonstrated to effectively reduce the local current density [23]. Carbon substrates such as doped graphene [24] and carbon black [25] have also been shown to be reasonably lithiophilic. However, these carbons with high surface areas come at a price of low initial CE. We ultimately chose to use graphite as it has good Li affinity and a low surface area. Electrochemically, the CE increases from 99.2% on Cu to 99.4% on graphite after initial

**FIGURE 3**

SEM images of Li deposited on Bi-Gr substrate in $\text{LiPF}_6\text{-mixTHF}$ electrolyte at different areal capacity, and corresponding charge/discharge curve and EDS elemental mapping images.

cycles (Fig. S2d). From the overpotential comparison (Fig. S3), it's obvious that graphite substrate has cut the overpotential by more than half, from 50 mV on Cu to 20 mV on graphite. However, after taking a closer look at the discharge curves, there is still a dip at the beginning of the Li deposition, indicating a noticeable Li nucleation barrier. It is known that Li metal alloys have good Li affinity which can act as 'Li glue' that can lead to an increase in CE [26]. From various metals, bismuth (Bi) was chosen because of its low expansion at full lithiation, which makes it easier for stable cycling. Slurry coated Bi electrode was tested as Li deposition substrate and exhibited excellent CE of 99.75+% (Fig. S2f), however the Bi capacity decayed in first 50 cycles and then remained relatively stable (Fig. S2e). To improve the substrate electrochemical stability, Bi and graphite was mixed and coated on Cu as substrate (Bi-Gr electrode). Elemental mapping (Fig. S4) clearly indicates the good dispersion of Bi microparticle on graphite substrate.

We initially evaluated the Li stripping/plating behavior and Li deposition morphologies on the designed Bi-Gr substrate in $\text{Li}||\text{Bi-Gr}$ cells with 2.0 M $\text{LiPF}_6\text{-mixTHF}$ electrolyte. A three-step reaction during Li plating/stripping process was observed (Fig. 3 and S3) corresponding to Bi alloying/dealloying, graphite Li intercalation/deintercalation, and Li plating/stripping. The short plateau at approximately 0.7 V is attributed to Li-Bi alloying. However, the sloping range from 0.2 to 0 V associated with Li intercalation of graphite is absent in the discharge curve because of the slow kinetics of graphite intercalation (Fig. S3), the signature golden color at initial lithiation (Fig. 3, photo labeled (1)) indicates the existence of stage I graphite intercalation compound. The absence of typical co-intercalation of ether into graphite results from the poor solvation strength of the mixTHF.

The dominant long plateau around 0 V is attributed to Li depositing/dissolution. It is worth noting that Bi-Gr substrate showed no spike at initial lithiation (Fig. S3). The charge/discharge curves overlap well (Fig. 4a), indicating (1) Bi-Gr substrate is stable and (2) there is not much overpotential increase over the 200 testing cycles. More importantly, the CE reaches 99.83+% at 0.5 mA cm^{-2} and 1.0 mAh cm^{-2} , much better than 99.2% on Cu foil tested under the same conditions.

To elucidate the underlying mechanism of the Bi-Gr substrate, SEM images and corresponding EDS mappings were acquired at different Li deposition areal capacities (Fig. 3). The initial 0.1 mAh cm^{-2} of Li is deposited on the periphery of Bi particles. It should be noted that while graphite provides more than 10 times the surface area, Li still preferentially deposits on Bi particles, verifying the strongly preferred nucleation of Li metal on Li-Bi alloy. Successive deposition of Li to 0.5 mAh cm^{-2} results in lateral growth from the deposited Li islands. At this level it is obvious that all the Li deposited is centered with Bi particle, demonstrating that the Li is grown from the Li-Bi alloy. Further deposition to 1.0 mAh cm^{-2} Li deposition leads to connection of Li island. After delithiation, no visible Li remained on the substrate, as shown in SEM images, indicating good reversibility of the lithiation/delithiation cycle on the Bi-Gr substrate. In the absence of Bi, Li nucleates and grows uniformly on graphite (Fig. S5). The morphology is similar at 1.0 mAh cm^{-2} Li deposition, only with the minor difference of the absent Bi particles.

Li plating/stripping on Bi-Gr substrate with 2 M $\text{LiPF}_6\text{-mixTHF}$ electrolytes

The high CE of 99.83+% is achieved through the combined effect of lithiophobic LiF-rich SEI formation and lithiophilic Bi-Gr sub-

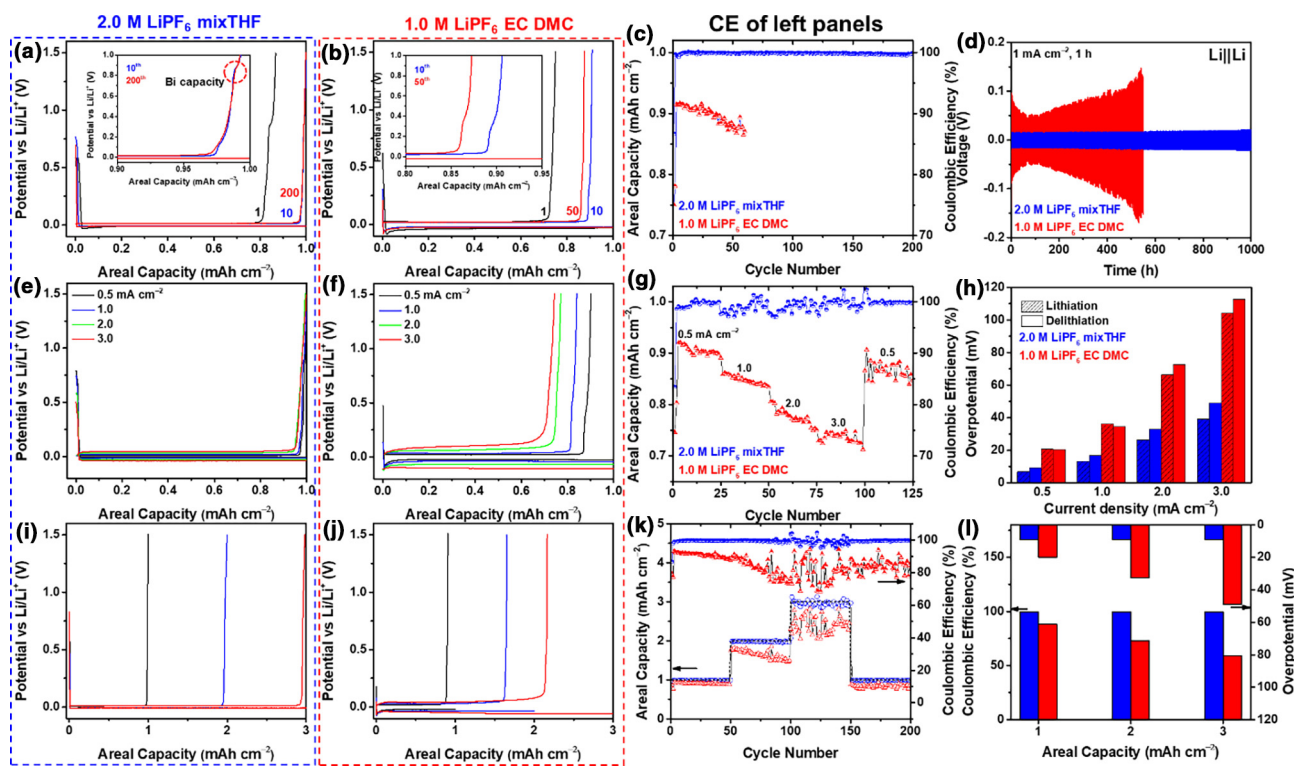


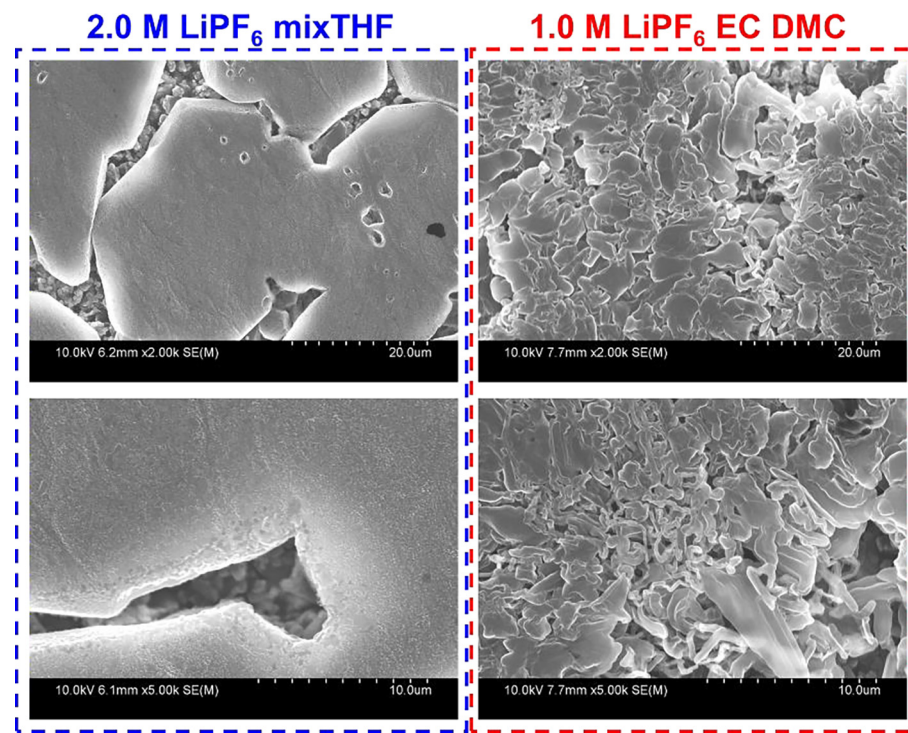
FIGURE 4

Electrochemical performance of Li-metal plating/stripping on a Bi–Gr Working Electrode in LiPF_6 –mixTHF (a, e, i, and blue) or EC/DMC (b, f, j, and red) electrolytes. (a and b) 0.5 mA cm^{-2} and 1.0 mAh cm^{-2} cycling, (e and f) rate testing with 1.0 mAh cm^{-2} capacity, (i and j) areal capacity test with 0.5 mA cm^{-2} current density, (c, g and k) corresponding cycling CE and capacities. (d) Voltage profiles for $\text{Li}||\text{Li}$ symmetrical cells, (h) overpotential at different current densities, (l) CE and overpotential comparison in areal capacity tests.

strate since the Bi–Gr substrate in LiPF_6 –EC/DMC still yields a low CE of $\sim 90\%$ (Fig. 4b and c), and the Cu foil in LiPF_6 –EC/DMC shows even worse CE ($\sim 86\%$). Detailed SEM and EDS mapping characterization (Fig. S6) of Li deposited on Bi–Gr substrate in LiPF_6 –EC/DMC electrolyte indicates more Li remained on the substrate after delithiation, which is reflected by the lower CE. Electrochemically, the excellent kinetics of the Li metal in LiPF_6 –mixTHF electrolyte was further studied in $\text{Li}||\text{Bi–Gr}$ half cells at various current densities with fixed lithium plating capacity (1.0 mAh cm^{-2}) and compared with commercial LiPF_6 –EC/DMC electrolyte (Fig. 4). The stable and nearly identical charge–discharge potential profiles with limited increasing hysteresis is observed for LiPF_6 –mixTHF electrolyte (Fig. 4e), which is in sharp contrast to the obviously decreasing CE and increasing hysteresis in LiPF_6 –EC/DMC electrolyte (Fig. 4f). The CE difference between these two electrolytes became larger when current density increased from 0.5 to 3.0 mA cm^{-2} (Fig. 4g). With the increase of current density, the CEs of $\text{Li}||\text{Bi–Gr}$ half cells in LiPF_6 –mixTHF electrolyte remain high values and still achieved 99.5% at 3.0 mA cm^{-2} , suggesting its superior reversibility at high rates. By contrast, the efficiency of $\text{Li}||\text{Bi–Gr}$ half cells in LiPF_6 –EC/DMC decreases quickly and hovers around only 70% at 3.0 mA cm^{-2} , indicating an accelerated Li dendrite and ‘dead Li’ generation at high current densities. The evolution of average voltage hysteresis at all current densities is presented in Fig. 4h. The overpotential during Li plating/stripping on Bi–Gr increases

with the current density in both electrolytes. But the changes in mixTHF electrolyte are not as significant as in a commercial LiPF_6 –EC/DMC electrolyte, especially at higher current density, and the voltage polarization of Li plating/stripping in LiPF_6 –mixTHF electrolyte is always less than half of those observed in commercial LiPF_6 –EC/DMC electrolyte. The reduced voltage hysteresis in LiPF_6 –mixTHF electrolyte is ascribed to the reduced SEI impedance, while the high CE indicates stable LiF-rich SEI formation and uniform Li plating/stripping in LiPF_6 –mixTHF electrolyte, even at high current densities.

To evaluate the potential of the Bi–Gr substrate in LiPF_6 –mixTHF electrolyte for practical applications with high areal capacities, Li plating/stripping half-cell tests at high capacity of 2.0 and 3.0 mAh cm^{-2} were also performed. Typical charge/discharge curves in the two electrolytes are shown in Fig. 4i and j. As was the case in rate tests, higher CE and lower hysteresis was observed in all test conditions in the LiPF_6 –mixTHF electrolyte. The potential hysteresis was unchanged as Li capacity increases from 1.0 to 3.0 mAh cm^{-2} in LiPF_6 –mixTHF electrolyte, indicating a stable interface even at high areal capacities. Conversely, the hysteresis of $\text{Li}||\text{Bi–Gr}$ cell in LiPF_6 –EC/DMC electrolyte increases with areal capacity, especially at the end of charge/discharge, indicating an unstable interface at high areal capacities. The evolution of an unstable interface also results in extremely unstable CE at higher areal capacities (Fig. 4k), indicating chaotic growth of Li after the areal capacity reaches a certain

**FIGURE 5**

SEM images of Li deposited on Bi-Gr substrate at 0.5 mA cm^{-2} and 1.0 mAh cm^{-2} in different electrolytes as noted.

value in $\text{LiPF}_6\text{-EC/DMC}$ electrolyte. This produced a sharp difference in CE observed at 3.0 mAh cm^{-2} : 99.5% (in $\text{LiPF}_6\text{-mixTHF}$) versus 59.3% (in $\text{LiPF}_6\text{-EC/DMC}$) (Fig. 4l).

SEM images and corresponding EDS mappings (Fig. S7) of deposited Li in $\text{Li}||\text{Bi-Gr}$ half cells at different current densities were acquired. It is obvious that with increasing current densities, the average size of Li island decreases, indicating that more nuclei formed at the beginning of Li deposition. The smaller size of Li islands leads to higher surface area exposing to electrolyte, which reduces the CE. Fortunately, the surface of the Li islands remained smooth and uniform regardless of the current densities and island size, as demonstrated in Fig. S7. The surface morphology of Li metal after 1.0 mAh cm^{-2} of Li deposited on Bi-Gr substrate in different electrolytes is distinctly different. As shown in Fig. 5, deposited Li is disk-like and with a smooth surface in $\text{LiPF}_6\text{-mixTHF}$, while it is nodule-like with some dendrite-like structures in $\text{LiPF}_6\text{-EC/DMC}$. The dendritic Li leads to more exposed Li surface area and generation of “dead Li”, caused by the continuous drop of Li plating/stripping CE in commercial $\text{LiPF}_6\text{-EC/DMC}$ electrolyte. SEM images (Fig. S8) show the Li metal coverage on Bi-Gr is increasing from 2.0 and 3.0 mAh cm^{-2} , also with higher degree of coalescence. Magnified SEM images of deposited Li on Bi-Gr in $\text{LiPF}_6\text{-mixTHF}$ electrolyte (Fig. S8) indicate no significant increase in surface roughness or dendrite growth at 2.0 and 3.0 mAh cm^{-2} . These stable and smooth Li metal surfaces contributed to the constant potential hysteresis at increasing areal capacity.

Cycling stability of $\text{Li}||\text{Li}$ symmetrical cells.

The cycling performance of Li metal in two electrolytes was examined using $\text{Li}||\text{Li}$ symmetrical cells at a current of

1.0 mA cm^{-2} and a capacity of 1.0 mAh cm^{-2} (Fig. 4d). Gradual decrease and then increase of voltage hysteresis with cycling is observed in the case of $1 \text{ M LiPF}_6\text{-EC/DMC}$, with very different shape of the charge/discharge curve for the 1st and 250th cycle (Fig. S9a and S9b). For initial cycles, the curve shape indicates dendritic growth of Li and subsequent removal of Li from dendrites and surface pitting [27], while the curve after 250 cycles indicates the accumulation of dead Li which forms a tortuous interphase [28]. The initial decrease in voltage hysteresis results from an increase in surface area that reduces impedance in competition with the continuous growth of SEI layer that increases impedance. The reduction in interfacial resistance during the initial 50 cycles in Fig. 4d is also verified by the continuously decreasing impedance over the first 50 cycles (Fig. S9c and S9d), during which the Li surface area increases significantly, developing porous and needle-like Li structure (Fig. S10). In contrast, much more stable cycling performance up to 1000 h (Fig. 4d) as well as almost unchanged hysteresis (Fig. S9a and S9b) and impedance (Fig. S9c and S9d) can be obtained in the $\text{Li}||\text{Li}$ cells with $\text{LiPF}_6\text{-mixTHF}$ electrolyte. This can be attributed to stable SEI formation and uniform and non-dendritic Li deposition (Fig. S10). Moreover, the enlarged voltage profiles of symmetric cells display a much lower voltage polarization and smoother plateaus in $\text{LiPF}_6\text{-mixTHF}$ than that in the $\text{LiPF}_6\text{-EC/DMC}$ electrolyte (maximum value 20 mV versus 400 mV (Fig. 4d and S9), indicating homogeneous Li plating/stripping and enhanced charge transfer kinetics.

Cycling stability of Li metal-free LiFePO_4 (LFP)||Bi-Gr full cell

The electrochemical stability window of 2.0 M LiPF_6 mixTHF electrolyte is $0.0\text{--}4.2 \text{ V}$ [29] allowing LiFePO_4 cathode to stably

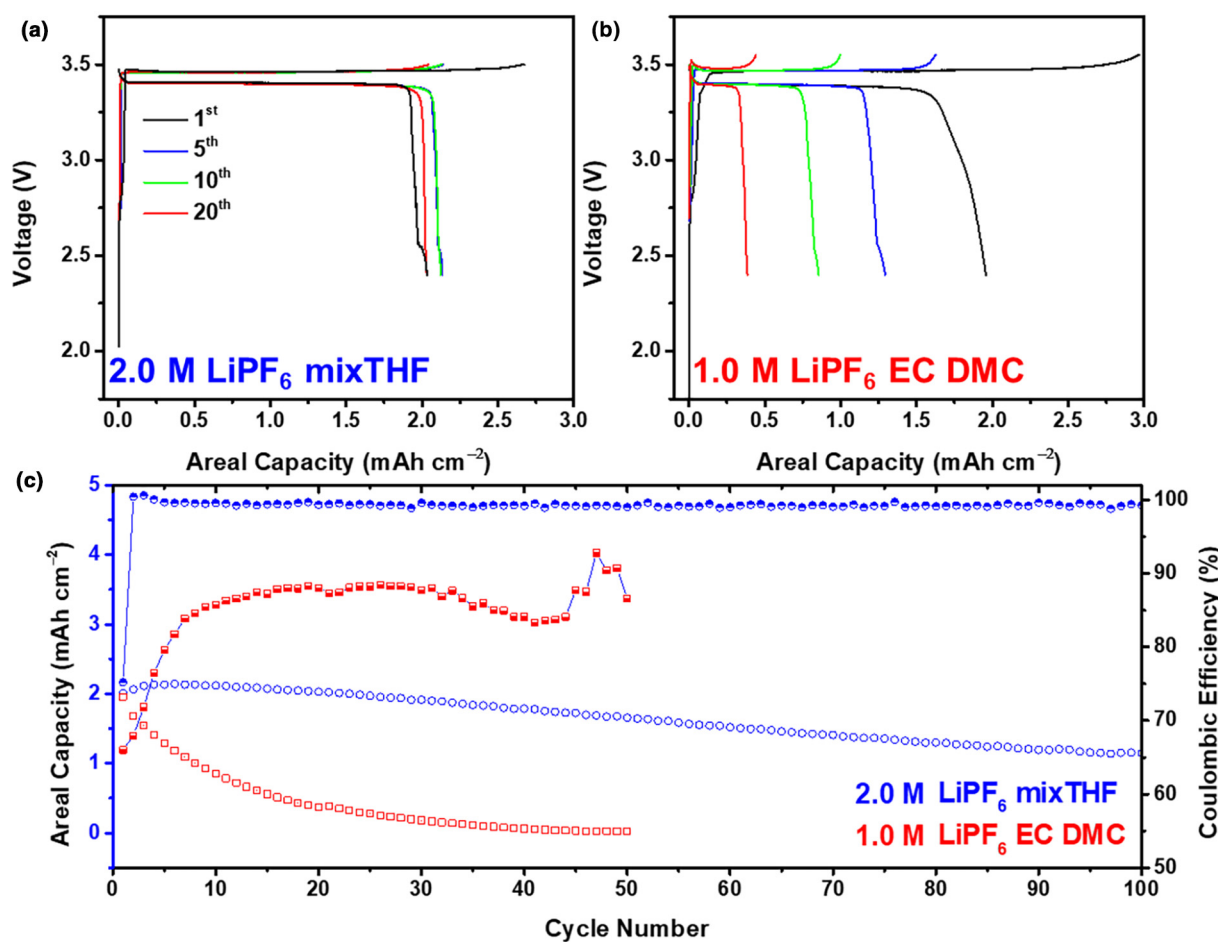


FIGURE 6

Li metal-free LFP||Bi-Gr full cell performance. (a and b) typical charge/discharge curves in (a) LiPF_6 -mixTHF and (b) LiPF_6 -EC/DMC electrolyte, and (c) corresponding CE and discharge capacities.

charged/discharged (Fig. S11). Bi-Gr||LiFePO₄ (LFP) full cells with high areal capacity ($>2.0\text{ mAh cm}^{-2}$) of LFP cathode and no Li metal or pre-lithiation anode were assembled to evaluate the performance in real applications (Fig. 6). This Li metal-free configuration is the ultimate form of Li metal battery (LMB) and does not require special environmental control other than typical prevailing dry room. The LiPF_6 -mixTHF electrolyte is capable of 100 cycles with CE close to 100%, while the capacity drops below 80% in LiPF_6 -EC/DMC electrolyte within 4 cycles with CE only $\sim 85\%$. This is one of the best reported cycling stabilities of LMB with anode-free configuration and high areal capacity ($>2.0\text{ mAh cm}^{-2}$) without additional external pressure, which highlights the benefits of a combined effort in both electrolyte and substrate design.

Conclusions

In summary, we successfully increased the cycling CE of Li metal by rational design of LiPF_6 -mixTHF electrolyte and Bi-Gr substrate, achieving the highest ever reported value of 99.83%+ at 0.5 mA cm^{-2} and 1.0 mAh cm^{-2} in Li||Bi-Gr half cells. The underlying mechanisms for Li dendrite suppression by lithiophobic LiF-rich SEI and for improving nucleation and adhesion by lithiophilic Bi-Gr substrate are theoretically and experimen-

tally demonstrated. These improvements are incorporated into anode-free full cells with LFP cathode and achieve 100 cycles with a practical areal capacity of $>2.0\text{ mAh cm}^{-2}$. The strategy reported here could provide new directions on the development of advanced anode-free LMBs.

CRediT authorship contribution statement

Ji Chen: Conceptualization, Writing - original draft, Writing - review & editing, Visualization, Methodology, Validation, Investigation. **Qin Li:** Methodology, Validation, Investigation. **Travis P. Pollard:** Methodology, Investigation. **Xiulin Fan:** Conceptualization, Validation. **Oleg Borodin:** Conceptualization, Writing - original draft, Writing - review & editing, Supervision, Methodology, Funding acquisition. **Chunsheng Wang:** Conceptualization, Writing - original draft, Writing - review & editing, Supervision, Funding acquisition.

Acknowledgements

This work was supported by the US Department of Energy (DOE) under award No DEEE0008202. We thank the Maryland NanoCenter and its AIMLab for characterization support. The modeling part of this work conducted at ARL was supported by the Joint Center for Energy Storage Research (JCESR), a Depart-

ment of Energy, Energy Innovation Hub, under cooperative agreement number W911NF-19-2-0046.

Author contributions

J.C. and Q. L. contributed equally to this work. J.C. and C.W. conceived the idea for the project. J.C. and Q. L. prepared the materials and performed electrochemical experiments. T.P. P. and O. B. conducted MD and BOMD simulations. X.F. helped with electrolyte preparation. All the authors discussed the results, analyzed the data and drafted the manuscript.

Appendix A. Supplementary data

Supplementary data to this article can be found online at <https://doi.org/10.1016/j.mattod.2020.04.004>.

References

- [1] J.-M. Tarascon, M. Armand, Issues and challenges facing rechargeable lithium batteries, in: Materials for Sustainable Energy: A Collection of Peer-Reviewed Research and Review Articles from Nature Publishing Group, World Scientific, 2011, p. 171.
- [2] Y. Gao et al., *Nat. Mater.* 18 (4) (2019) 384.
- [3] L. Suo et al., *Nat. Commun.* 4 (2013) 1481.
- [4] C. Fang et al., *Nature* 572 (7770) (2019) 511, <https://doi.org/10.1038/s41586-019-1481-z>.
- [5] X. Chen et al., *Sci. Adv.* 5 (2) (2019) eaau7728, <https://doi.org/10.1126/sciadv.aau7728>.
- [6] H. Ye et al., *Angew. Chem. Int. Ed.* 58 (4) (2019) 1094.
- [7] Q. Li, S. Zhu, Y. Lu, *Adv. Funct. Mater.* 27 (18) (2017) 1606422.
- [8] H. Ye et al., *Adv. Energy Mater.* 7 (23) (2017) 1700530.
- [9] W. Liu et al., *Adv. Energy Mater.* 9 (2019) 1802918, <https://doi.org/10.1002/aenm.201802918>.
- [10] X. Fan et al., *Sci. Adv.* 4 (12) (2018) eaau9245, <https://doi.org/10.1126/sciadv.aau9245>.
- [11] X. Cao et al., *Nat. Energy* 4 (9) (2019) 796.
- [12] X. Fan et al., *Nat. Nanotechnol.* 13 (8) (2018) 715, <https://doi.org/10.1038/s41565-018-0183-2>.
- [13] S.-J. Cho et al., *iScience* 23 (2) (2020), <https://doi.org/10.1016/j.isci.2020.100844>.
- [14] J.L. Goldman et al., *J. Electrochem. Soc.* 127 (7) (1980) 1461, <https://doi.org/10.1149/1.2129931>.
- [15] X.Q. Zhang et al., *Adv. Funct. Mater.* 27 (10) (2017) 1605989, <https://doi.org/10.1002/adfm.201605989>.
- [16] O. Borodin, *Curr. Opin. Electrochem.* 13 (2019) 86, <https://doi.org/10.1016/j.jcoelec.2018.10.015>.
- [17] D. Strmcnik, *Nat. Catal.* 1 (4) (2018) 255, <https://doi.org/10.1038/s41929-018-0047-z>.
- [18] D. Dong, *PCCP* 20 (46) (2018) 29174.
- [19] O. Borodin et al., *Joule* 4 (1) (2020) 69, <https://doi.org/10.1016/j.joule.2019.12.007>.
- [20] P. Ganesh, P.R.C. Kent, D.E. Jiang, *J. Phys. Chem. C* 116 (46) (2012) 24476, <https://doi.org/10.1021/jp3086304>.
- [21] X. Ji et al., *Nano Today* 7 (1) (2012) 10.
- [22] R. Mukherjee et al., *Nat. Commun.* 5 (2014) 3710.
- [23] R. Zhang et al., *Adv. Mater.* 28 (11) (2016) 2155.
- [24] R. Zhang et al., *Angew. Chem. Int. Ed.* 56 (27) (2017) 7764.
- [25] H. Liu et al., *ACS Appl. Energy Mater.* 1 (5) (2018) 1864, <https://doi.org/10.1021/acsaem.8b00348>.
- [26] S.S. Zhang, X. Fan, C. Wang, et al., *Electrochim. Acta* 258 (2017) 1201.
- [27] K.N. Wood et al., *ACS Centr. Sci.* 2 (11) (2016) 790.
- [28] K.-H. Chen et al., *J. Mater. Chem. A* 5 (23) (2017) 11671.
- [29] J. Chen et al., *Nat. Energy* (2020), <https://doi.org/10.1038/s41560-020-0601-1>.